

Orientation-dependent extreme shear strain in single-crystalline silicon - from elasticity to fracture

Carmen M. Lauener^{a,*}, Fabian Schwarz^a, Laszlo Pethö^b, Jeffrey M. Wheeler^a, Johann Michler^b, Ralph Spolenak^a

^a Laboratory for Nanometallurgy, ETH Zurich, Vladimir-Prelog-Weg 5, Zurich, 8093, Switzerland

^b Mechanics of Materials and Nanostructures, Empa, Feuerwerkerstrasse 39, Thun, 3602, Switzerland

ARTICLE INFO

Keywords:

Micro shear testing
Digital image correlation
Elastic strain measurement
Anisotropic elasticity

ABSTRACT

Measuring strain accurately at small length scales poses a significant challenge, making it difficult to obtain precise elastic properties of small materials. This becomes particularly pronounced for test geometries beyond micro-pillars and for materials with high elastic limits and high Peierls stresses. This study investigates the elastic strain limits and strain distribution in micro double shear tests conducted on single-crystalline silicon with different crystallographic orientations. *In situ* scanning electron microscopy images were used to obtain full-field strain maps using digital image correlation. This local strain analysis approach revealed that the shear zones of the test geometry are not solely under pure shear conditions, but also experience superimposed bending. The local strain analysis approach increases the precision of measured elastic properties to $\pm 15\%$ of the literature value compared to deviations of 75–80% using the traditional global strain analysis approach. This study highlights the limitations of the global strain analysis approach in complex specimen geometries and demonstrates the effectiveness of digital image correlation in accurately determining elastic strain at the small length scale. Furthermore, both the low defect density in the samples as well as the small length scales allow for the exploration of orientation dependent strength levels close to the theoretical limit.

1. Introduction

Silicon (Si) is an ubiquitous material in computing and mobile devices. Small structures made out of Si serve as both functional and structural components in microelectromechanical systems. In these devices, components often are subjected to multiaxial loading [1,2]. Additionally, the observation of micro-scale plasticity in Si at room temperature [3,4] has prompted further inquiries into the fatigue mechanism of Si. This mechanism may be attributed to dislocation glide and plastic deformation [5]. Shear not only represents a simple case of multiaxial loading, but it also is the driving force of dislocation glide processes. Thus, direct shear measurement is desirable as a small scale materials testing technique.

Recently, a micro double shear (MDS) geometry has been successfully applied to investigate the behavior of specific shear systems in metals [6–9]. The MDS geometry consists of a central loading section, two constricted shear zones and two outer support parts (see Fig. 1c). During uniaxial loading of the central section with a nanoindenter, this

specimen geometry transforms the far-field uniaxial compression into a simple shear stress state in the shear zones. The advantage of the MDS geometry is that it allows a specific shear/slip system of interest to be subjected to direct shear deformation up to high strains without rotation of slip planes. For example, Au [6] and Cu [7] single crystals were deformed to shear strains larger than 100% without change in slip geometry. This is contrary to uniaxial compression [10–12] or tension [13], where the sample geometry changes profoundly during plastic deformation and the activation of secondary slip systems occurs. Plastic deformation in MDS experiments of metals occurs via the formation of a new shear band or with a sudden deformation in an existing shear band. However, the formation of a shear band in only one shear zone can break the symmetry of the MDS test geometry and subsequent activation of alternative slip planes occurs or even ductile tearing is observed [9]. Additionally, local differences (presence of pre-existing defects in the respective shear zone) and/or misalignment may result in a stress transfer from one shear zone to the other [6,7], however, direct experimental observation of this phenomenon is missing.

* Corresponding author.

E-mail address: carmen.lauener@mat.ethz.ch (C.M. Lauener).

<https://doi.org/10.1016/j.matdes.2023.112423>

Received 14 July 2023; Received in revised form 19 October 2023; Accepted 19 October 2023

Available online 24 October 2023

0264-1275/© 2023 The Author(s). Published by Elsevier Ltd. This is an open access article under the CC BY license (<http://creativecommons.org/licenses/by/4.0/>).

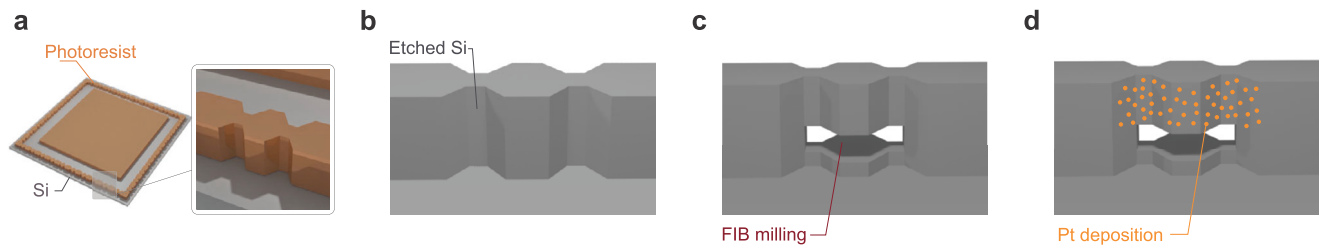


Fig. 1. Fabrication process for MDS specimens. (a) Photoresist was spun on silicon chips and patterned using direct laser writing. (b) Reactive ion etching creates walls with shear zones. (c) Focused ion beam milling releases the structure. (d) Application of Pt speckles using electron beam deposition for DIC contrast.

The deformation behavior of silicon differs significantly from that of metals. The directional nature of silicon's strong covalent bonds results in significant resistance to dislocation motion (high Peierls stress) [14,15] at room temperature, resulting in a high elastic limit before deformation via fracture instead of plasticity occurs. Consequently, for MDS testing of materials with high strengths and high elastic limits it is unlikely that the estimated pure shear strain by global strain analysis is actually the case. Therefore, the global strain analysis approach used in micromechanical test methodology, where the strain is calculated from measured displacement and critical dimensions of the test specimen, is limited and unsuited to accurately determine elastic properties, such as the shear modulus. A local strain analysis in the shear zone is required to accurately determine shear strains.

To address this challenge and quantify deformation at the micrometer or sub-micrometer length scale, digital image correlation (DIC) has been applied to scanning electron microscopy (SEM) images [16–18]. This enabled new insights into the deformation mechanism of metals [19–21], residual stresses of thin coatings [22], and achieve a higher level of precision in determining critical resolved shear stresses of pillar compression experiments [23]. These studies focused on plasticity, while our unique application of sequential digital image correlation on *in situ* SEM images may provide a solution to the intricate problem of accurately characterizing elastic strains at small length scales.

The present work explores the application of MDS testing to materials with high Peierls stresses. Shear testing was performed on two different crystallographic shear systems of single-crystalline Si: $\{110\}\langle 00\bar{1} \rangle$ and $\{\bar{1}11\}\langle \bar{1}\bar{1}0 \rangle$. We demonstrate full-field strain measurements at the micrometer-scale using digital image correlation, which enables the assessment of local shear strains in the shear zones of MDS specimen. Those results were compared to global strains obtained from micro-compression test methodology. Based on this, individual compliance contributions on measured deformations were evaluated and are presented in an analytical model. We report the influence of different strain calculation methods on the interpretation of the stress-strain response. The elastic stress-strain response of the two crystal orientations is compared to literature values. This study gives insight into the elastic strain limits of silicon under shear loading at the small length scale.

2. Experimental details

2.1. Material, orientations and specimen fabrication

Micro double shear (MDS) specimens were fabricated in single-crystalline Si using a combined approach of photolithography techniques and focused ion beam (FIB) milling, see Fig. 1. Two silicon wafers (4 in. diameter, P/B-doped) with $\langle 001 \rangle$ and $\langle 110 \rangle$ out-of-plane orientations, respectively, served as substrate materials. MDS specimens were fabricated with two selected orientations to enable activation of different slip systems: $\{110\}\langle 00\bar{1} \rangle$ and $\{\bar{1}11\}\langle \bar{1}\bar{1}0 \rangle$, with the nomenclature {shear plane} and \langle shear direction \rangle . We refer to the respective sample by using their out-of-plane orientation.

Initially, a direct laser writer (MLA 150, Heidelberg Instruments GmbH) was used to create the MDS design on the photo-resist (AZ ECI

3027, Microchemicals GmbH) coated wafers (Fig. 1a). After development (AZ 400 K, Microchemicals GmbH), an anisotropic dry etch using the Bosch process (Omega Rapiet, SPTS Technologies) created a wall-like structure with defined shear zones close to the edge of the silicon substrates (see Fig. 1b). MDS specimens were undercut by FIB milling using a Helios 600i Gallium FIB (Thermo Fisher Scientific), as shown in Fig. 1c. A milling current of 2.5 nA was used for coarse rectangular cuts, while a milling current of 0.77 nA was used for final dimensioning cuts near the bottom of the specimens.

For DIC, electron beam deposition (Fig. 1d) was used to apply a platinum (Pt) speckle pattern on an area of $10 \times 20 \mu\text{m}^2$ on the side of the specimens following the protocol as described in [20]. The MDS geometry proposed by Heyer et al. [6] was modified in order to enable digital image correlation by creating better visibility of the shear zone. This was achieved by removing excess material from the central loading section and the outer support parts.

2.2. Mechanical testing and global strain analysis

The micro-shear experiments were performed *in situ* inside a LEO 1530 (Carl Zeiss AG) scanning electron microscope (SEM), using a Alemnis standard assembly system (Alemnis AG) [24]. The system was equipped with a diamond flat punch tip (Synton-MDP LDT) of $8 \mu\text{m}$ in diameter. The MDS specimen was compressed in the central section of the geometry using a constant displacement rate of 10 nm/s . During compression of the structure *in situ* images were acquired with a cycle time of 2.62 s for digital image correlation. An acceleration voltage of 5 kV and beam current of 200 nA was used. Scan width of $18.75 \mu\text{m}$, resulting in a pixel size of 18.31 nm . Six specimens of each orientation were tested until failure. On three additional specimens, load-unload cycles were performed to increasing displacements.

Engineering stresses and strains were obtained from the measured load-displacement data and the dimensions of the MDS specimen. Each shear zone is defined by its width W , a depth D , and a height H , as shown in Fig. 2. Engineering stresses are obtained from the applied load P as

$$\tau = \frac{P}{2HD} \quad (1)$$

Engineering shear strains are obtained from the measured shear displacement Δ as

$$\gamma = \frac{\Delta}{W} \quad (2)$$

Stress-strain curves obtained from compression data will be referred to as global strain analysis in the following.

2.3. Digital image correlation and local strain analysis

Two-dimensional DIC was performed on the *in situ* SEM images with the software VIC-2D [25]. A subset size of 33×33 pixel with a step size of 8 pixel was used. If necessary, one seeding point was defined manually in order to assist the correlation process. The strain resolution was measured from static SEM images (no load applied) acquired over a time frame of 2 min which corresponds to the experimental time of the

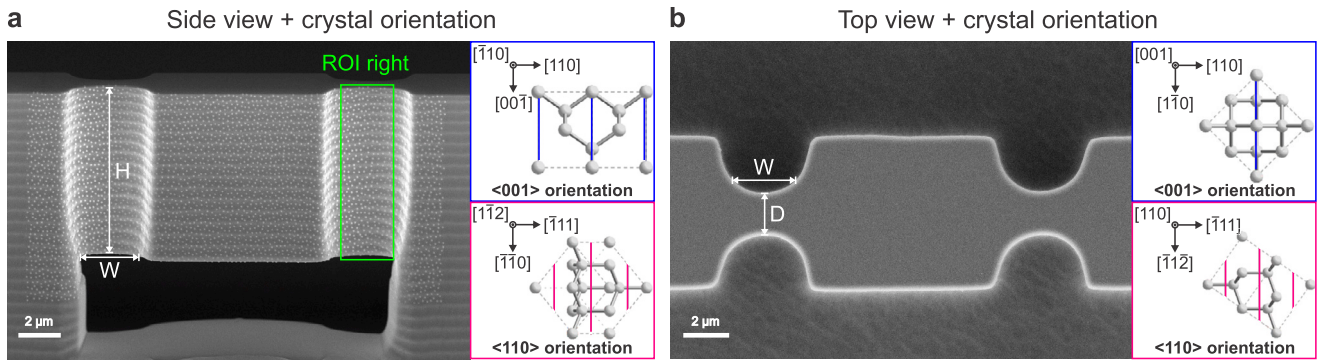


Fig. 2. In-lens SEM images of final MDS specimen. Dimensions ($H = 8 \mu\text{m}$, $W = 2.5 \mu\text{m}$, and $D = 1.8 \mu\text{m}$) and crystal orientation of the two shear systems are indicated. (a) Tilted side view: The Pt speckles are clearly visible and show high contrast to the silicon background. (b) Top view: Corner rounding effect is apparent. D was determined at narrowest section.

conducted MDS tests. As a conservative estimate we report the largest false strain found for ϵ_{yy} after 2 min. We obtained a strain resolution of $7 \times 10^{-4} \pm 3 \times 10^{-3}$, which includes the error introduced due to SEM drift distortions. The reported noise (1-standard-deviation) is constant over time. Color-coded strain maps depict engineering strains computed from the Lagrange strain tensor. A $2.5 \mu\text{m}$ wide rectangle defined the region-of-interest for each shear zone. The average shear strain was extracted from these regions to conduct the local strain analysis.

2.4. Finite element analysis

Finite element modeling (FEM) of the shear geometry was performed in COMSOL Multiphysics® v. 6.0. [26]. The FEM simulation assumes anisotropic elastic material behavior for silicon. The elastic constants of single-crystalline silicon are $c_{11} = 165.7 \text{ GPa}$, $c_{12} = 63.9 \text{ GPa}$ and $c_{44} = 79.6 \text{ GPa}$ [27]. The stiffness tensor was rotated using AniCryDe [28] to align the axes with the crystallographic orientation of interest. The indenter was modeled implicitly by applying step-wise displacements at the contact-area between the shear specimen and the indenter. The boundary conditions were adapted such that the FEM displacement field resembles the DIC displacement output. The shear stresses and strains were extracted from the surface of the shear zone. For more comprehensive details, please refer to the supplementary information.

3. Results

3.1. Micro double shear geometry

Fig. 2 shows SEM images of the MDS specimen produced by a combined approach of lithography etching and FIB milling. The Pt speckles provide high contrast on the Si surface and are clearly distinguishable from the background (see Fig. 2a). Vertical etching using standard lithography processing techniques result in reproducible dimensions and straight side walls. However, some rounding of the corners occurs, due to the finite width of the laser beam (about $1 \mu\text{m}$) used for patterning, as shown in Fig. 2b. For the shear zones, a depth D of $1.8 \mu\text{m}$ (measured at the narrowest section), a height H of $8 \mu\text{m}$, and an average shear width of $2.5 \mu\text{m}$ were determined. Consequently, the underestimation of the area supporting the applied load causes overestimation of the shear stresses calculated using equation (1). The cut out for the shear zone was made larger (100° compared to 90°), which resulted in good visibility of the shear zone in SEM images and makes DIC possible. Full-field strain maps were obtained for the entire speckled area. A region-of-interest (ROI) was established for both the left (ROI left) and right (ROI right) shear zones (as indicated in Fig. 2a, only ROI right is shown). The average shear strain was extracted from these regions to conduct the local shear strain analysis.

3.2. Digital image correlation and local strain analysis

Fig. 3 shows the results of the DIC analysis for the two shear systems during the progression of a MDS test. The strain distributions of engineering shear strains (Fig. 3a) and normal strains (Fig. 3b) at various stress levels are shown. Upon compression of the central section with a flat punch (Fig. 3, left to right), a shear stress state is induced in the two shear zones. As a Cartesian system axis was utilized, shear strain values in the left shear zones have negative values, while shear strains in the right shear zones are positive. Table 1 summarizes the absolute average shear strain values obtained for the left (ROI left) and right (ROI right) shear zone. For both orientations, the left shear zone experiences smaller shear strains compared to the right shear zone. At the same shear stress, samples with a $\langle 110 \rangle$ orientation show higher shear strain values compared to samples with a $\langle 001 \rangle$ orientation. The highest shear strains initially develop in the middle of the respective shear zone, then with further compression they extend diagonally from the lower corner close to the support parts towards the upper corner close to the central section.

Fig. 3b shows the corresponding strain distribution of normal strains (ϵ_{xx}) obtained from the DIC analysis. Generally, normal strains are much lower compared to shear strains at the same stress level as designed. Significant bending occurs at the corners of the shear zones and peak values are located at the corners closest to the flat punch.

Fig. 4 compares the results obtained from DIC and FEM analysis. Fig. 4a shows the displacement along the compression axis. The central section experiences the highest displacement (average value of $1.028 \pm 0.025 \mu\text{m}$), which agrees well with the uncorrected displacement measured by the nanoindenter (max. value of $1.063 \mu\text{m}$). The outer supports show a displacement of $\sim 650 \text{ nm}$ along the compression axis, due to system and sample compliance. Fig. 4b and c compare the corresponding shear strain distribution and normal strain distribution of DIC and FEM analysis. While the DIC results show a strain transfer from the left to the right shear zone, the FEM results show a symmetric shear strain distribution in the shear zones. At the top and the bottom of the shear zone the superimposed bending of the structure dominates and shear strains vanish. Normal strains extend from the corners of the shear zone and are the highest at the corners closest to the flat punch. Contrary to FEM results, the DIC strain map shows more pronounced normal strains in the corners towards the outer support parts.

Fig. 5 presents the results of line profiles obtained by evaluating 200 points of a horizontal line in the middle of the geometry, as indicated in Fig. 4. Every fifth frame of the DIC analysis is shown and compared to the FEM results obtained for a set displacement of $1 \mu\text{m}$. FEM results were extracted from the midplane of the MDS geometry. The line profiles of the displacement map along the compression axis shown in Fig. 5a illustrate two important results. First, the displacement of the middle section is slightly asymmetric with higher displacements at positive X-positions. This is in agreement with higher shear strain values

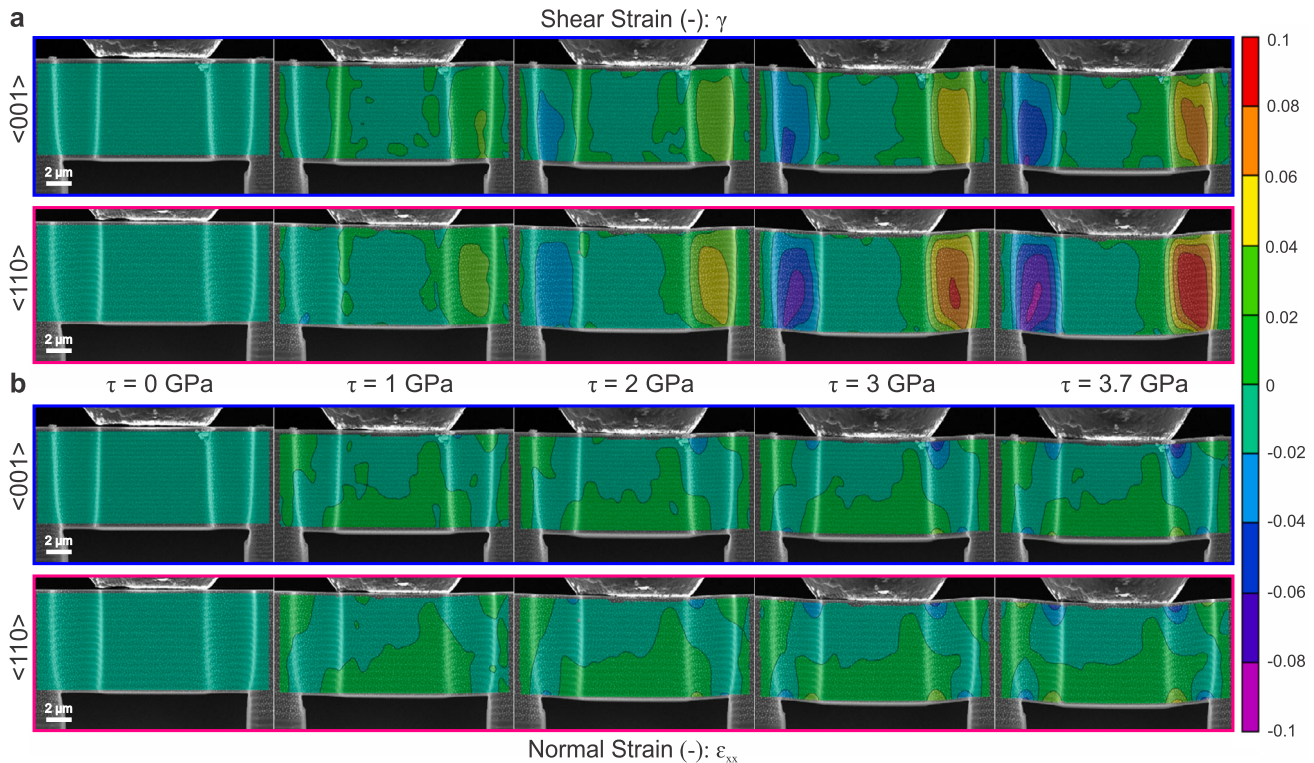


Fig. 3. Strain distribution at different shear stresses. DIC color maps of (a) engineering shear strains and (b) normal strains.

Table 1

Local shear strains in the shear zones determined using DIC strain maps shown in Fig. 3.

Shear stress (GPa)	$\langle 001 \rangle$ orientation			$\langle 110 \rangle$ orientation		
	ROI left (%)	ROI right (%)	Average (%)	ROI left (%)	ROI right (%)	Average (%)
1.0	0.6 ± 0.6	1.4 ± 0.6	1.0 ± 0.8	1.3 ± 0.5	2.0 ± 0.5	1.6 ± 0.7
2.0	1.5 ± 0.9	2.7 ± 0.8	2.1 ± 1.2	2.8 ± 0.9	4.0 ± 1.0	3.4 ± 1.3
3.0	2.6 ± 1.2	4.2 ± 1.0	3.4 ± 1.6	4.7 ± 1.5	6.4 ± 1.5	5.6 ± 2.1
3.7	3.5 ± 1.4	5.3 ± 1.3	4.4 ± 1.9	6.0 ± 1.7	7.9 ± 1.9	7.0 ± 2.5

obtained for the right shear zone (Fig. 5b). Second, the displacement along the compression axis of the outer support parts makes the system and substrate compliance apparent. Line profiles of shear strain maps show that shear strain values are the highest in the middle of the shear zone. For the left shear zone shear, strain values peaked at 8%, while the average shear strain obtained for ROI left was 6% (Table 1). Similarly, for the right shear zone a maximum value of 10% shear strain was obtained, while the average shear strain was at 7.9%.

3.3. Global and local stress-strain response

Fig. 6a shows load-displacement results of the MDS test for the two shear systems over three loading cycles. Except for the initial loading section, the force increases linearly with displacement. Upon unloading, the load decreases linearly following the loading curve with a small hysteresis. During the third loading cycle, a sudden load drop occurs when the specimen fractures. Fig. 6b show three stress-strain curves of each orientation. The global stress-strain response obtained from machine-compliance-corrected load-displacement data vastly overestimates shear strains and consequently significantly deviate from the literature stiffness of each crystal orientation. Further, the experimental spread is larger compared to differences caused by the crystal's anisotropy. The local stress-strain response was obtained from matching the average DIC strain of both shear zones with the stress data obtained from the global analysis. Local stress-strain curves show clear differ-

ences in the elastic response of the two crystal orientations and are in good agreement with literature values.

3.4. Failure morphology

As the small differences in the elastic behavior are challenging to observe, we present the fracture surfaces of several of the MDS structures. Fig. 7 shows SEM images of MDS specimens after failure. In silicon single crystals, cleavage preferentially occurs on $\{111\}$ or $\{110\}$ planes [29,30]. As shown in Fig. 7, brittle fracture occurs on $\{111\}$ cleavage planes, regardless if these planes are aligned for shear or not. For the $\langle 001 \rangle$ orientation, the fracture morphology is consistent for different specimens and is symmetric in both shear zones. One main crack on $\{111\}$ planes, which have an angle of 54.7° to the $\langle 001 \rangle$ surface, for each shear zone is clearly visible, as shown in Fig. 7a. Pinpointing the source of these cracks presents a formidable task. However, it's worth noting that the most prominent cracks appear to meet at the edge of the flat punch, suggesting that stress concentrations between the flat punch and the sample surface may be responsible for initiation of fracture. For the $\langle 110 \rangle$ orientation, the right shear zone shows a main crack parallel to the compression axis while the left shear zone shows crack deflection over several crystalline planes, as shown in Fig. 7b. This fracture morphology implies that failure occurs first in the right shear zone on $\{111\}$ cleavage planes. This is consistent with higher strains measured in the right shear zone (compare Fig. 3). In this scenario, where the crack morphology aligns parallel to the compression axis, the initia-

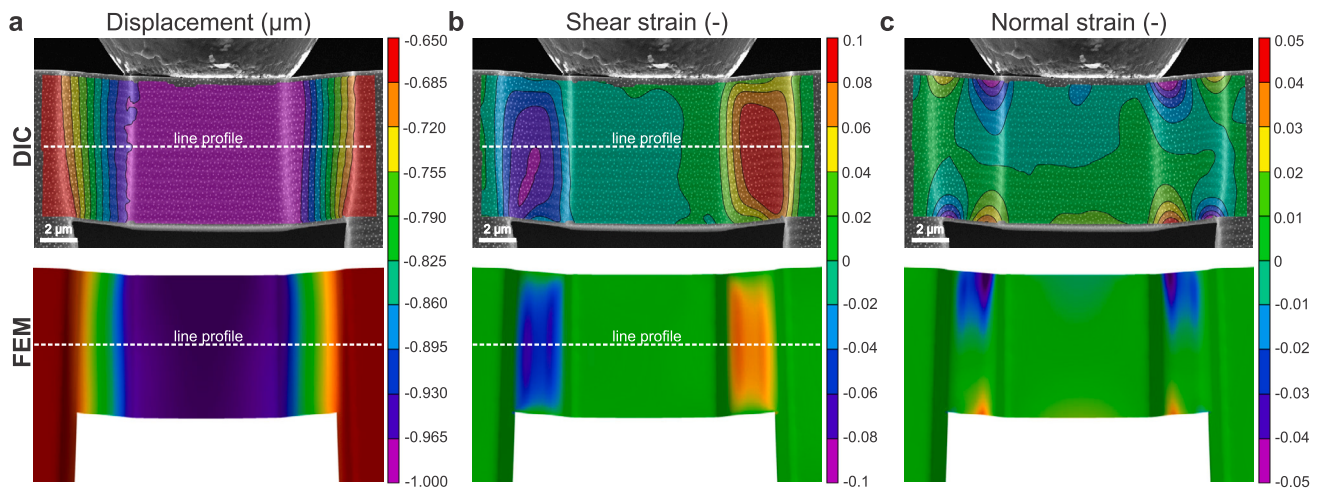


Fig. 4. Comparison of results acquired from DIC and FEM. (a) Displacement along compression axis. (b) Distribution of shear strains. (c) Distribution of normal strains.

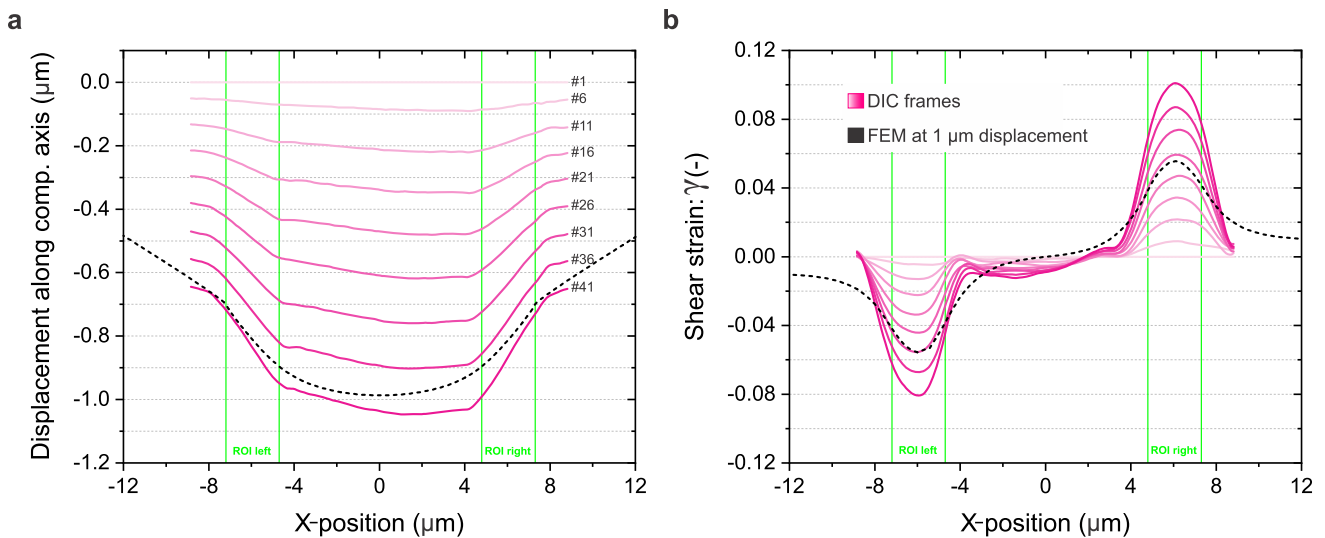


Fig. 5. Line profile analysis of horizontal lines across the displacement map and shear strain distribution map (shown in Fig. 4). DIC data is shown in pink and every fifth frame is displayed. FEM line profile for a displacement of 1 μm is shown as a black dashed line. (a) Line profiles for the displacement along compression axis. (b) Corresponding line profiles showing shear strains.

tion of fracture could potentially be affected by the damage layer at the bottom surface of the shear zone, which is a result of FIB milling [31].

4. Discussion

4.1. Strain distribution in MDS testing

In this study, we conducted MDS tests on single crystalline silicon with two different crystallographic orientations. We utilized *in situ* SEM images to obtain full strain maps by means of DIC. As shown in Fig. 3, the color-coded strain distribution maps illustrate that pure shear conditions were not achievable for high elastic limit silicon. Instead, the upper and lower regions of the shear zone are impacted by superimposed bending. Although this phenomenon was predicted by FEM studies [6], we present unique direct experimental measurements of this phenomenon via DIC. Using the results presented in Fig. 3a and b at a global shear stress of 3.7 GPa, we find that ~40% ($\langle 001 \rangle$ orientation) and ~66% ($\langle 110 \rangle$ orientation) of the shear zone, respectively, is at a homogeneous shear strain state ($>4\%$ shear strain and $<1\%$ normal strain). This is in good agreement with our FEM results where a homogeneous shear strain is present in ~32% ($\langle 001 \rangle$ orientation) and

~44% ($\langle 110 \rangle$ orientation) of the shear zone. This reduction in area of homogeneous shear strain compared to simple metals (~80% [6]) is a consequence of the material's high Peierls stresses and high elastic limit. Bending strains are predominantly observed in the corners of the shear zone and are more pronounced in corners closer to the central loading section. This aligns with beam bending theory for double-cantilevered beams, where the highest bending moments are in the vicinity of the loading point [32].

A significant variation from FEM is the asymmetric distribution of shear strain values between the two shear zones during an actual experiment (Fig. 4). As the symmetry of the MDS geometry forces the two shear zones to deform in parallel, both shear zones are expected to experience the same shear displacement. However, in all experiments, the shear strain values are consistently higher in the right shear zone than in the left shear zone (Table 1). This is the case for all specimens of both orientations. We attribute this artifact to misalignment between the flat punch and the sample surface. Additionally, line profiles of the displacement along the compression axis support this theory, as the displacement at positive relative X-positions is consistently higher compared to negative X-positions (Fig. 5a). We assume that the flat punch makes first contact in the right part of the central loading sec-

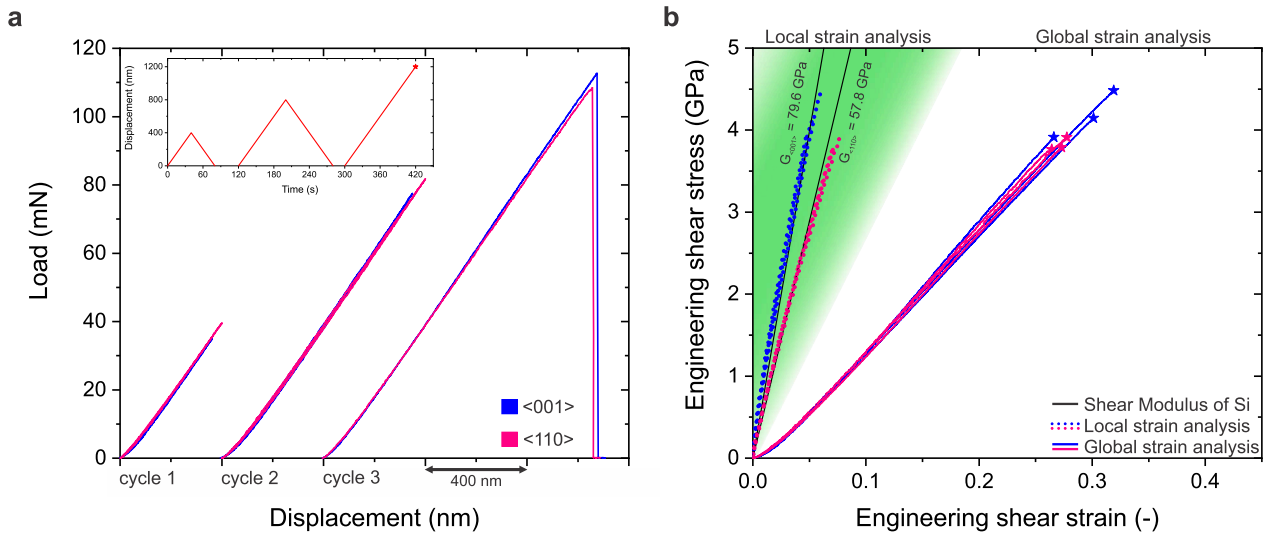


Fig. 6. Mechanical response of the two shear orientations. (a) Load-displacement curves of three loading cycles. The inset shows the loading profile. (b) Multiple stress-strain curves for both crystal orientations. For the local strain analysis (green background) average shear strain values of both shear zones were used.

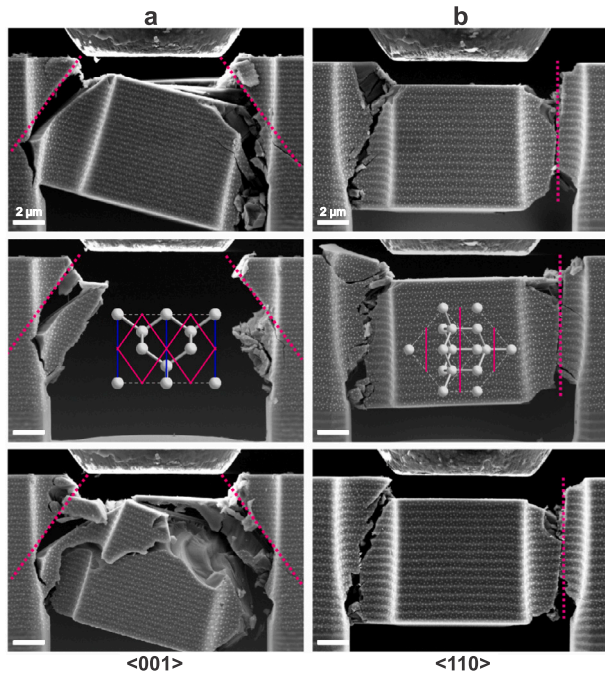


Fig. 7. In-lens SEM images of MDS specimen after failure. Crystal lattice orientation is illustrated in middle image, where selected {111} planes are shown in pink and {110} planes are shown in blue. (a) For specimen with <001> orientation fracture occurs on inclined {111} planes. (b) For specimen with <110> orientation fracture occurs on {111} planes in the right shear zone.

tion (i.e. positive X-positions). This causes the initial non-linearity in the load-displacement data. Consequently, line profiles of shear strain maps (Fig. 5b) show asymmetric peak shear strain values. The surface shear strain value obtained through FEM for a set displacement of 1 μm appears to be lower than the shear strain determined by DIC. This difference can be attributed to the adjustments made to the boundary conditions of the FEM simulation, aligning them with the displacements recorded through DIC. The disparity results from inherent variations between experiment and FEM simulation. Factors such as the significant compliance introduced by the load cell and misalignment are aspects not accounted for in the FEM simulations.

The ratio of shear strain values of the shear zones ($\gamma_{\text{left}}/\gamma_{\text{right}}$) varies in the beginning of the experiment and then plateaus at a constant value of 0.64 ± 0.04 (<001> orientation) and 0.73 ± 0.02 (<110> orientation). The larger ratio obtained for the <110>-oriented crystal is expected, since this orientation has a lower shear modulus and thus transfers strain easier from one shear zone to the other. We used the obtained strain ratios in order to estimate the misalignment using our FEM model. By tilting the flat punch tip in the xz-plane, we found that a tilt of $\sim 3^\circ$ (<001> orientation) and $\sim 2^\circ$ (<110> orientation) away from the ideal loading axis results in the above mentioned shear strain ratios of the respective orientation. As the flat punch was not unmounted between testing the two different crystal orientations, the difference of $\sim 1^\circ$ in misalignment is associated with misalignment introduced while mounting the Si chip on the SEM stub and/or fixing the SEM stub in the indenter system.

4.2. Global and local strain assessment

The standard approach in micromechanical test methodology is to convert load-displacement data to engineering stress-strain curves (global strain analysis). This presumes a uniform strain distribution in the deformed volume and includes subtracting various compliance contributions from the measured deflection. MDS specimen of both orientations were loaded reproducibly in the elastic regime over three loading cycles without any significant change in loading stiffness (Fig. 6a). As expected, Si behaved purely elastically until brittle fracture occurred. Stress-strain curves obtained for the local and global strain analysis are displayed in Fig. 6b. For MDS experiments, a simple global strain analysis is not effective to determine materials properties in the elastic regime, since this results in shear strains that are considerably overestimated (by a factor of 3.2 resp. 5). This is a result of various compliances within the complex sample geometry, which in this case only produced a relatively small area of uniform shear strain. Further, the spread between different specimens of the same orientation is larger than the anisotropic stress-strain response of different crystal orientations. Hence, a simple global strain analysis is unable to distinguish the difference in the elastic stress-strain response of the two shear orientations.

Local strain assessment using DIC is more effective and insightful. The difference in shear modulus between the different orientations ($\sim 27\%$) is evident. This demonstrates that local strain analysis with DIC allows elastic anisotropy to be examined, as well as accurately

Table 2

The maximum shear strength, shear strain, and shear modulus obtained from the global and local strain analysis approach.

	Index	Global strain analysis			Local strain analysis			
		τ_{max} (GPa)	γ_{max} (%)	G (GPa)	γ_{left} (%)	γ_{right} (%)	avg. γ (%)	G (GPa)
(001) orientation	1	3.4	27.6	13.3	2.5	4.2	3.4	87.3
	2	3.8	27.9	14.5	3.2	5.6	4.4	75.4
	3	4.1	30.1	14.4	4.0	6.4	5.2	71.2
	4	3.6	26.5	14.7	3.3	5.2	4.2	74.2
	5	4.5	31.9	14.5	4.7	7.2	6.0	68.4
	6	3.8	25.8	15.4	3.8	5.4	4.6	71.1
	7	4.0	27.1	15.4	3.9	5.7	4.8	70.8
	8	4.3	28.4	16.1	4.2	6.4	5.3	71.0
	9	3.9	26.6	15.8	3.7	5.7	4.7	73.0
	Average	3.9 ± 0.3	22.6 ± 7.7	14.9 ± 0.9	3.7 ± 0.7	5.8 ± 0.8	4.7 ± 0.7	73.6 ± 5.6
(110) orientation	A	3.9	27.8	14.8	6.6	8.7	7.6	46.4
	B	3.8	27.3	14.7	6.1	8.1	7.1	48.4
	C	3.6	26.3	14.5	5.2	7.3	6.2	52.2
	D	3.9	26.2	15.5	6.1	8.7	7.4	46.4
	E	3.7	27.7	14.4	6.0	8.3	7.2	47.8
	F	3.9	27.4	15.0	6.2	8.4	7.3	49.2
	G	3.8	26.4	15.2	6.0	7.9	7.0	49.1
	H	3.6	25.3	15.3	5.6	7.7	6.7	49.4
	I	3.1	22.5	15.3	4.5	6.4	5.4	52.8
	Average	3.7 ± 0.2	21.8 ± 6.7	15.0 ± 0.4	5.8 ± 0.6	7.9 ± 0.8	6.9 ± 0.7	49.1 ± 2.3

determining the local strain at failure. Strain values obtained for all specimens are enlisted in Table 2.

The large influence of the strain assessment methods is displayed in Fig. 8a. Here, we present stress-strain curves obtained from uncorrected load-displacement data along with different compliance corrections. The machine compliance of $0.0036 \mu\text{m}/\text{mN}$ was determined experimentally and accounts for about 37% of the total measured deformation (uncorrected displacement). Moreover, it is evident that the substrate and sample geometry's bending compliance significantly influences the measurement. To attempt to improve upon the simple global strain analysis, we derived an analytical model to estimate their individual contributions using the geometry of a simple double-cantilevered beam with a uniform depth \bar{D} of $3.7 \mu\text{m}$ (see supplementary information). For the substrate's contribution to the measured deformation, we used Sneddon's criterion for the indentation of a flat punch into an infinite half space as follows:

$$\Delta_{\text{substrate}} = \frac{P(1-\nu)}{4\mu a} = \frac{P(1-\nu^2)}{2Ea} \quad (3)$$

where the rigidity modulus is defined as $\mu = E/2(1+\nu)$ with E the Young's modulus, ν the Poisson ratio, and a is the radius of the circle of contact. For the simple beam $a = \bar{D}/2$ and for the Young's modulus we used 130 GPa and for the Poisson ratio 0.28 ((001) orientation) and 169 GPa and 0.36 ((110) orientation), respectively. We find that the substrate contribution to the total measured deformation is about 20% ((001) orientation) and 14% ((110) orientation), respectively.

For the sample geometry's bending contribution to the measured deformation, we used the displacement for bending of a double-cantilevered beam with a point load in the middle, which is defined as:

$$\Delta_{\text{bending}} = \frac{PL^3}{192EI} \quad (4)$$

where L is the length of the beam, and the area moment of inertia $I = 1/12H^3D$ with H and D representing the height and depth of the beam, respectively. By using a beam length L of $16 \mu\text{m}$, a height H of $8 \mu\text{m}$, an uniform depth \bar{D} of $3.7 \mu\text{m}$, and the same respective Young's modulus as mentioned above, we find that the bending contribution to the total measured deformation is about 11% ((001) orientation) and 8% ((110) orientation), respectively.

The resulting stress-strain curves using these analytical corrections are presented in Fig. 8a. After the analytical corrections the stress-strain curves can distinguish the anisotropy in the elastic response with only

an error of $\sim 1\%$. However, the obtained stiffness still deviates about 57% from literature values. Larger corrections using a more narrow beam, would result in a non-deterministic relation of stress and strain (i.e. curve bends over), due to the initial non-linear stress-strain response. As the MDS geometry is significantly more complex than these analytical approximations, it is not surprising that the resulting correction still falls short of ideal expectations. This highlights the necessity and importance of DIC as an alternative method to accurately determine strain of complex small-scale test geometries.

Fig. 8b summarizes the obtained average shear moduli using the two strain assessments for different loading cycles. Shear moduli were obtained from stress-strain curves by fitting the second half of the curves obtained from the global strain analysis (machine compliance corrected) and the local strain analysis. Generally, moduli obtained from unloading curves are slightly higher compared to the ones obtained from loading curves. The global strain analysis shows a constant shear modulus regardless of the loading cycle. An average shear modulus of 14.9 ± 0.9 GPa ((001) orientation) and 15.0 ± 0.4 GPa ((110) orientation) were obtained, and hence the anisotropy in shear modulus could not be resolved.

In the case of the local strain analysis, shear moduli are overestimated in the first loading cycle then plateau out below the respective literature value. Moduli obtained from average shear strain values for the (001) orientation (73.6 ± 5.6 GPa) deviate about 8% and for the (110) orientation (49.1 ± 2.3 GPa) about 15% from the respective literature shear modulus. The initial overestimation of the modulus is associated to an artifact of averaging over the entire shear zone in combination with a lack of DIC output data for fitting, i.e. only 8 data points for loading cycle 1. All results are summarized in Table 3.

4.3. Shear strength and comparison to pillar compression tests

To examine the statistical behavior of the shear failure strength, as it occurs by stochastic fracture, individual shear strengths and their failure probability are presented in form of a Weibull plot (Fig. 9a). The two shear orientations show comparable distributions (i.e. similar Weibull slopes) and comparable Weibull moduli of 4.1 GPa ((001) orientation) and 3.8 GPa ((110) orientation), respectively. This indicates good reproducibility of the MDS tests. Si pillars of similar size exhibit a slightly higher Weibull shape parameter of about 20 [33]. The larger variation found in MDS tests compared to pillar compression might stem from stress concentrations caused by cut-outs of the test geometry or by misalignment.

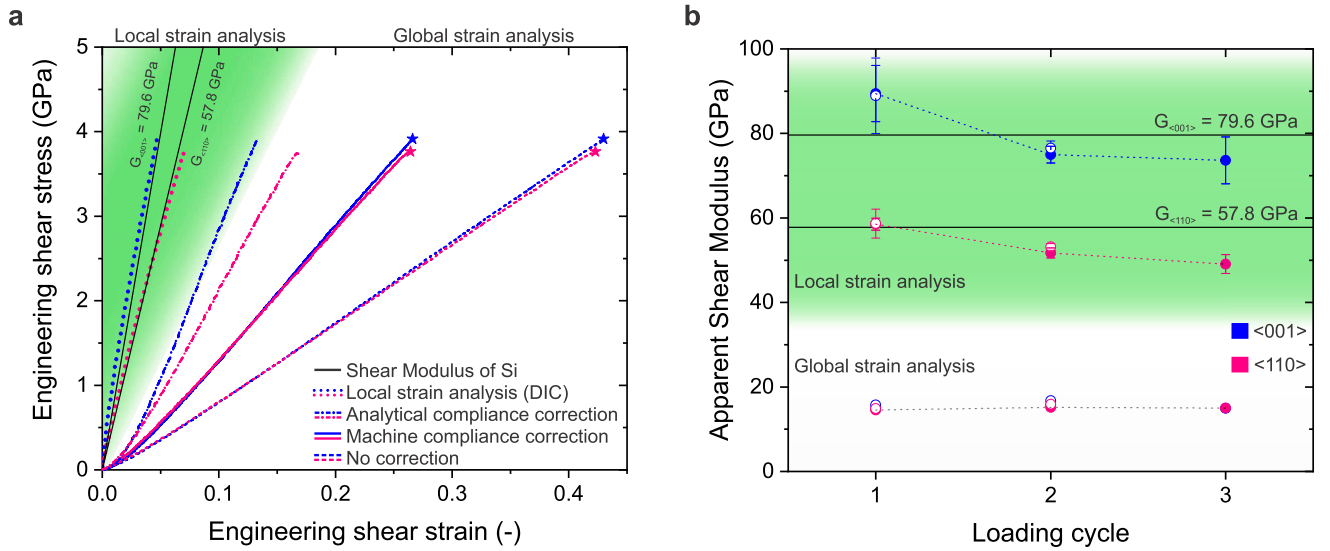


Fig. 8. Elastic properties of MDS experiments. (a) Stress-strain curves obtained using different strain assessments. The literature values of the respective orientation are shown as black solid lines. (b) Shear moduli obtained for the local and global strain assessments. Open symbols represent values obtained from unloading curves, and closed symbols are obtained from loading curves.

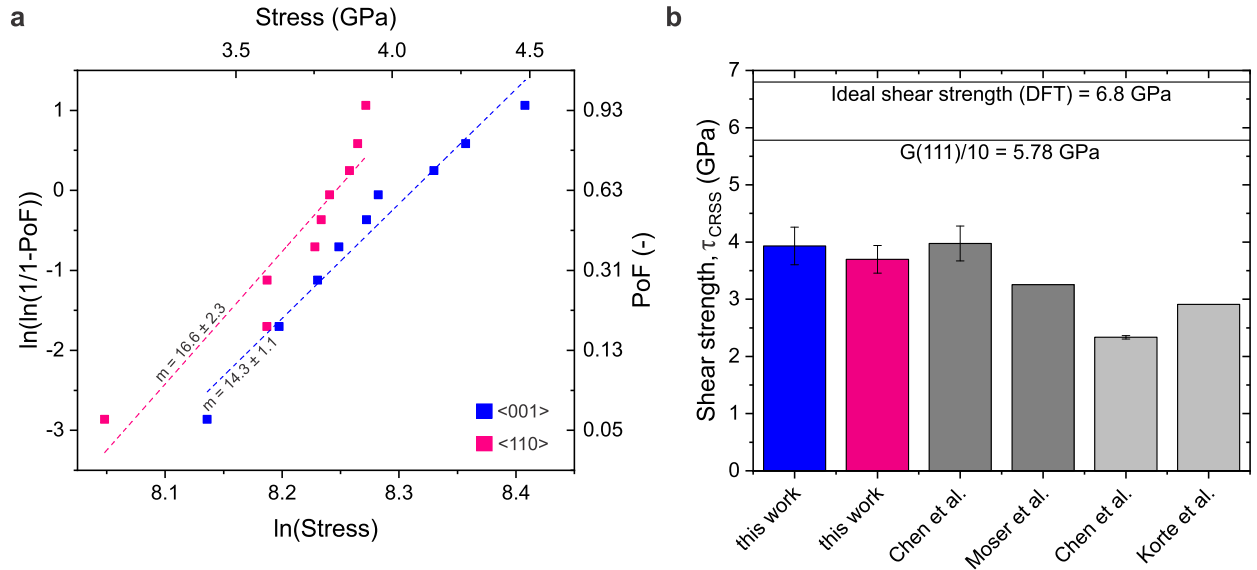


Fig. 9. Measured shear strengths of MDS experiments. (a) Weibull plot (b) Comparison of average shear strength obtained in this work to critical resolved shear stresses obtained by pillar compression [4,33,34]. All pillars have a $\langle 001 \rangle$ orientation; dark gray: lithography pillars, light gray: FIB pillars.

Table 3
Mechanical data obtained for the two crystal orientations.

Orientation	$\langle 001 \rangle$	$\langle 110 \rangle$
Literature shear modulus [GPa]	79.6 [27]	57.8 [35]
Global shear modulus [GPa]	14.9 ± 0.9	15.0 ± 0.4
Local shear modulus [GPa]	73.6 ± 5.6	49.1 ± 2.3
Maximum shear strength [GPa]	3.9 ± 0.3	3.7 ± 0.2
Weibull slope [-]	14.3 ± 1.1	16.6 ± 2.3
Weibull modulus [GPa]	4.1	3.8
$\gamma_{local}/\gamma_{global}$ [-]	0.20 ± 0.02	0.31 ± 0.02

The shear strength obtained for the $\langle 001 \rangle$ orientation (3.9 ± 0.3 GPa) and the $\langle 110 \rangle$ orientation (3.7 ± 0.2 GPa) reach a large fraction of the ideal strength of Si ($\sigma_{ideal} = G/10$, where G is the shear modulus of the respective shear system [35,27]), as shown in Fig. 9b. Density functional theory suggests a higher theoretical maximum shear strength of 6.8 GPa [36] to 8 GPa [37] for the $\{111\}$ plane, however, devia-

tion from linearity occurs at shear stresses of about 4.5 GPa. The shear strength obtained from MDS tests is in excellent agreement with the results obtained from pillar compression, where typically the critical resolved shear strength (CRSS) is extracted. For lithographic Si pillars [4,33] a CRSS of 4 GPa was obtained, while Si pillars fabricated by FIB [4,34] exhibit lower CRSS due to FIB damage. Nonetheless, this agreement in the obtained strength reinforces the reliability and effectiveness of pillar compression as a viable technique for evaluating the critical resolved shear strength of materials, despite the non-ideal shear stress state of a pillar in micro-compression.

Furthermore, it is anticipated that the study of plastic deformation in silicon under direct shear loading will become feasible by reducing specimen dimensions or conducting experiments at elevated temperatures [4,34]. This offers exciting opportunities for future research in this field.

5. Conclusions

In this work, a methodology for combining micro-shear testing with digital image correlation was successfully developed to measure the elastic anisotropy and fracture strength of single-crystalline silicon samples. Our approach pioneers the utilization of DIC within the elastic regime for *in situ* SEM experiments, enabling the precise characterization of elastic strains at small length scales. In conclusion, this study highlights the importance of local strain analysis compared to traditional *in situ* nanoindenter test setups and the associated global strain analysis approach in accurately determining elastic strain due to the dominating effect of compliance. We demonstrate that in this case the use of digital image correlation provides a significantly more accurate strain determination specifically for high-strength materials, even enabling the resolution of the small anisotropy in the shear modulus of different shear systems in silicon.

Beyond the accurate determination of elastic mechanical behavior the current approach also allows to access the brittle elastic limits for silicon at room temperature. Fracture tends to occur preferentially on {111} planes, even in cases where these planes are not specifically aligned as shear planes. These findings contribute to the advancement of understanding the complexities of strain measurements and deformation behavior in strong small-scale brittle materials.

CRedit authorship contribution statement

Carmen M. Lauener: Conceptualization, Investigation, Methodology, Visualization, Writing – original draft. **Fabian Schwarz:** Investigation, Methodology, Writing – review & editing. **Laszlo Pethö:** Methodology, Writing – review & editing. **Jeffrey M. Wheeler:** Conceptualization, Writing – review & editing. **Johann Michler:** Writing – review & editing. **Ralph Spolenak:** Conceptualization, Funding acquisition, Supervision, Writing – review & editing.

Declaration of competing interest

The authors declare that they have no known competing financial interests or personal relationships that could have appeared to influence the work reported in this paper.

Data availability

Data will be made available on request.

Acknowledgements

This project has received funding from the ETH Zurich Research Grants: ETH-40 19-1. The authors gratefully acknowledge ScopeM for their support & assistance in this work.

Appendix A. Supplementary material

Supplementary material related to this article can be found online at <https://doi.org/10.1016/j.matdes.2023.112423>.

References

- [1] T.R. Hsu, MEMS and Microsystems: Design and Manufacture, Mechanical Engineering Series, McGraw-Hill, 2002.
- [2] Nicolae Lobontiu, E. Garcia, Mechanics of Microelectromechanical Systems, Springer Science & Business Media, 2004.
- [3] A. Merabet, M. Texier, C. Tromas, S. Brochard, L. Pizzagalli, L. Thilly, J. Rabier, A. Talneau, Y.-M. Le Vaillant, O. Thomas, J. Godet, Acta Mater. 161 (2018) 54–60.
- [4] M. Chen, L. Pethö, A.S. Sologubenko, H. Ma, J. Michler, R. Spolenak, J.M. Wheeler, Nat. Commun. 11 (2020) 1–10.
- [5] H. Izumi, T. Kita, S. Arai, K. Sasaki, S. Kamiya, J. Mater. Sci. 57 (2022) 8557–8566.
- [6] J.K. Heyer, S. Brinckmann, J. Pfetzinger-Micklich, G. Eggeler, Acta Mater. 62 (2014) 225–238.
- [7] N. Wiecek, G. Laplanche, J.K. Heyer, A.B. Parsa, J. Pfetzinger-Micklich, G. Eggeler, Acta Mater. 113 (2016) 320–334.
- [8] G. Laplanche, N. Wiecek, F. Fox, S. Berglund, J. Pfetzinger-Micklich, K. Kishida, H. Inui, G. Eggeler, Acta Mater. 160 (2018) 173–184.
- [9] M.Y. Seok, H. Gopalan, S. Nandy, S. Zaefferer, D. Raabe, C. Kirchlechner, G. Dehm, Materialia 14 (2020) 100932.
- [10] R. Maaß, S. Van Petegem, D. Grolimund, H. Van Swygenhoven, D. Kiener, G. Dehm, Appl. Phys. Lett. 92 (2008).
- [11] R. Maaß, S. Van Petegem, C.N. Borca, H. Van Swygenhoven, Mater. Sci. Eng. A 524 (2009) 40–45.
- [12] C. Kirchlechner, J. Keckes, C. Motz, W. Grosinger, M.W. Kapp, J.S. Micha, O. Ulrich, G. Dehm, Acta Mater. 59 (2011) 5618–5626.
- [13] C. Kirchlechner, P.J. Imrich, W. Grosinger, M.W. Kapp, J. Keckes, J.S. Micha, O. Ulrich, O. Thomas, S. Labat, C. Motz, G. Dehm, Acta Mater. 60 (2012) 1252–1258.
- [14] L. Pizzagalli, P. Beauchamp, Philos. Mag. Lett. 84 (2004) 729–736.
- [15] Y. Kamimura, K. Edagawa, S. Takeuchi, Acta Mater. 61 (2013) 294–309.
- [16] M.A. Sutton, N. Li, D.C. Joy, A.P. Reynolds, X. Li, Exp. Mech. 47 (2007) 775–787.
- [17] M.A. Sutton, N. Li, D. Garcia, N. Cornille, J.J. Orteu, S.R. McNeill, H.W. Schreier, X. Li, A.P. Reynolds, Exp. Mech. 47 (2007) 789–804.
- [18] A.D. Kammers, S. Daly, Meas. Sci. Technol. 22 (2011).
- [19] F. Di Gioacchino, J. Quinta da Fonseca, Exp. Mech. 53 (2013) 743–754.
- [20] F. Di Gioacchino, W.J. Clegg, Acta Mater. 78 (2014) 103–113.
- [21] T.E.J. Edwards, F. Di Gioacchino, W.J. Clegg, Int. J. Fatigue 142 (2021) 105905.
- [22] M. Sebastiani, C. Eberl, E. Bemporad, G.M. Pharr, Mater. Sci. Eng. A 528 (2011) 7901–7908.
- [23] J.T. Pürstl, H.O. Jones, T.E. Edwards, R.P. Thompson, F. Di Gioacchino, N.G. Jones, W.J. Clegg, Mater. Sci. Eng. A 800 (2021) 140323.
- [24] J.M. Wheeler, J. Michler, Rev. Sci. Instrum. 84 (2013).
- [25] VIC-2D, version 6.0.6, Correlated Solution Inc., 2017.
- [26] COMSOL Multiphysics, version 6.0, COMSOL Inc., 2021.
- [27] M.A. Hopcroft, W.D. Nix, T.W. Kenny, J. Microelectromech. Syst. 19 (2010) 229–238.
- [28] R. Camattari, L. Lanzoni, V. Bellucci, V. Guidi, J. Appl. Crystallogr. 48 (2015) 943–949.
- [29] A. Misra, I. Finin, J. Mater. Sci. 14 (1979) 2567–2574.
- [30] G. Michot, Surf. Sci. Lett. 186 (1987) 561–567.
- [31] C.M. Lauener, L. Pethö, M. Chen, Y. Xiao, J. Michler, J.M. Wheeler, Mater. Des. 142 (2018) 340–349.
- [32] W.C. Young, R.G. Budynas, Roark's Formulas for Stress and Strain, McGraw-Hill Education, 1989.
- [33] B. Moser, K. Wasmer, L. Barbieri, J. Michler, J. Mater. Res. 22 (2007) 1004–1011.
- [34] S. Korte, J.S. Barnard, R.J. Stearn, W.J. Clegg, Int. J. Plast. 27 (2011) 1853–1866.
- [35] J. Kim, D.-i. Cho, R.S. Muller, Transducers '01 Eurosensors XV, 2001, pp. 662–665.
- [36] D. Roundy, M.L. Cohen, Phys. Rev. B, Condens. Matter Phys. 64 (2001) 2.
- [37] S.M.M. Dubois, G.M. Rignanese, T. Pardo, J.C. Charlier, Phys. Rev. B, Condens. Matter Phys. 74 (2006) 1–7.